Contrib Mineral Petrol (2017) 172:76
DOI 10.1007/s00410-017-1395-4

ORIGINAL PAPER

Timescales of mixing and storage for Keanakāko‘i Tephra magmas (1500–1820 C.E.), Kīlauea Volcano, Hawai‘i

Kendra J. Lynn[1,2] · **Michael O. Garcia**[1] · **Thomas Shea**[1] · **Fidel Costa**[3] · **Donald A. Swanson**[4]

Received: 27 February 2017 / Accepted: 16 July 2017

Abstract The last 2500 years of activity at Kīlauea Volcano (Hawai‘i) have been characterized by centuries-long periods dominated by either effusive or explosive eruptions. The most recent period of explosive activity produced the Keanakāko‘i Tephra (KT; ca. 1500–1820 C.E.) and occurred after the collapse of the summit caldera (1470–1510 C.E.). Previous studies suggest that KT magmas may have ascended rapidly to the surface, bypassing storage in crustal reservoirs. The storage conditions and rapid ascent hypothesis are tested here using chemical zoning in olivine crystals and thermodynamic modeling. Forsterite contents (Fo; [Mg/(Mg + Fe) × 100]) of olivine core and rim populations are used to identify melt components in Kīlauea's prehistoric (i.e., pre-1823) plumbing system. Primitive ($\geq$Fo$_{88}$) cores occur throughout the 300+ years of the KT period; they originated from mantle-derived magmas that were first mixed and stored in a deep crustal reservoir. Bimodal olivine populations ($\geq$Fo$_{88}$ and Fo$_{83-84}$) record repeated mixing of primitive magmas and more differentiated reservoir components shallower in the system, producing a hybrid composition (Fo$_{85-87}$). Phase equilibria modeling using MELTS shows that liquidus olivine is not stable at depths >17 km. Thus, calculated timescales likely record mixing and storage within the crust. Modeling of Fe–Mg and Ni zoning patterns (normal, reverse, complex) reveal that KT magmas were mixed and stored for a few weeks to several years before eruption, illustrating a more complex storage history than direct and rapid ascent from the mantle as previously inferred for KT magmas. Complexly zoned crystals also have smoothed compositional reversals in the outer 5–20 μm rims that are out of Fe–Mg equilibrium with surrounding glasses. Diffusion models suggest that these rims formed within a few hours to a few days, indicating that at least one additional, late-stage mixing event may have occurred shortly prior to eruption. Our study illustrates that the lifetimes of KT magmas are more complex than previously proposed, and that most KT magmas did not rise rapidly from the mantle without modification during shallow crustal storage.

Keywords Hawai‘i · Kīlauea · Magma storage · Olivine · Diffusion

Introduction

Kīlauea (Hawai‘i) is one of the best-studied volcanoes in the world (Tilling and Dvorak 1993; Garcia 2015), yet it has centuries-long periods of poorly understood explosive eruptions that may date back to ~70 ka (Easton and Garcia 1980; Easton 1987). Two centuries-long periods of explosive activity have occurred in the last 2500 years (Swanson

---

Communicated by Gordon Moore.

Electronic supplementary material The online version of this article (doi:10.1007/s00410-017-1395-4) contains supplementary material, which is available to authorized users.

✉ Kendra J. Lynn
kjlynn@udel.edu

[1] Department of Geology and Geophysics, University of Hawai‘i, Honolulu, HI 96822, USA

[2] Department of Geological Sciences, University of Delaware, Newark, DE 19711, USA

[3] Earth Observatory of Singapore, Asian School of the Environment, Nanyang Technological University, Singapore 639797, Singapore

[4] U.S. Geological Survey, Hawaiian Volcano Observatory, P.O. Box 51, Hawaii National Park, HI 96718, USA

et al. 2014). The most recent explosive period followed the collapse of the summit caldera, an event that can have significant impacts on the structure of a volcano's shallow magmatic reservoir system (Corbi et al. 2015), magmatic processes (e.g., fractional crystallization vs. magma mixing), and the geochemistry of erupted material (Gavrilenko et al. 2016). Explosive activity at Kīlauea may have ended around the time that western missionaries first visited in 1823 (Ellis 1827). The only historical records of these eruptions are translations of Hawaiian oral tradition (Swanson 2008). Thus, little is known about the magmatic processes operating in the crustal reservoir system during prehistoric (i.e., pre-1823) explosive periods.

The Keanakākoʻi Tephra (KT; ca. 1500–1820 C.E.) is the main unit produced during Kīlauea's most recent explosive period. The start date is approximate, based only on ^{14}C ages. The explosive period lasted until at least 1790 and possibly several decades later. We use a tentative end date of 1820 (Sharp et al. 1987), but acknowledge that sporadic phreatic and phreatomagmatic eruptions could have continued into the 1830s. The KT explosive period began during or just after the formation of the modern summit caldera (1470–1510 C.E.; Swanson et al. 2012a) and is Kīlauea's best exposed and most thoroughly studied tephra sequence (McPhie et al. 1990; Mastin 1997; Mastin et al. 2004; Swanson et al. 2012a, b, 2014, 2015; Helz et al. 2015). Vent locations for KT eruptions were probably geographically widespread across Kīlauea's summit region (Swanson et al. 2006, 2012b; May et al. 2015). The explosive KT eruptions were thought to result from rapid injection of magma into a deep crater wet with ground or surface water, causing extensive interactions between magma or hot rock and water (e.g., McPhie et al. 1990; Mastin 1997; Mastin et al. 2004). Recent work on olivine-hosted melt inclusions with inferred high-volatile contents have led to the interpretation that KT magmas ascended rapidly from mantle depths, bypassing crustal reservoirs to erupt explosively (Sides et al. 2014). Heterogeneous glasses (e.g., 6.5–11.0 wt% MgO) in several KT units were also interpreted to reflect inefficient mixing and little or no storage for the high-MgO magma in the reservoir system (Helz et al. 2014, 2015). To date, the mixing histories and the duration of crustal residence for KT magmas remain poorly known.

The storage and rapid ascent hypothesis is tested here by determining the petrological histories and quantifying the residence time for KT magmas from mixing to eruption. Chemical zoning in olivine phenocrysts provides a means to investigate the timing and duration of magma storage at shallow levels in volcanic systems (e.g., Costa and Dungan 2005). Diffusive re-homogenization of compositional differences in olivine can be modeled to extract timescales that record the interval between magma mixing events and eruption (e.g., Costa et al. 2008 and references therein). The KT sequence is ideal for investigations of Kīlauea's prehistoric crustal reservoir system because the tephras are glassy with heterogeneous MgO contents, indicating inefficient mixing of magmas (Swanson et al. 2014; Helz et al. 2015) and olivine crystals with adhering glass are present in almost all KT eruption deposits containing juvenile material.

The magmatic histories of eight KT samples are investigated here utilizing: (1) olivine core compositions; (2) modeling the diffusive re-equilibration of Fe–Mg and Ni in chemically zoned olivine, and (3) Fe–Mg disequilibrium between olivine rims and adhering glass. The melt components in which olivine phenocrysts grew (e.g., within primitive vs. evolved magmas) are determined from core composition populations. Distributions of olivine rim compositions are used to infer the melt composition in which crystals were stored prior to eruption. Zoning of Fe–Mg and Ni in these crystals provide timescales associated with mixing and storage before eruption. Together, these characteristics are used to determine the petrologic histories for KT magmas and describe Kīlauea's prehistoric plumbing system after the collapse of the summit caldera during a period of relatively low magma supply (Swanson et al. 2014).

Sample description and preparation

The Keanakākoʻi Tephra includes deposits from explosive phreatomagmatic and phreatic eruptions, high lava fountains, and one effusive lava flow (McPhie et al. 1990; Swanson et al. 2012a). Eight units with juvenile material spanning the entire KT period (ca. 1500–1820 C.E.) were included in this study (cf. Table 1 for brief unit descriptions). Six sites around Kīlauea's summit caldera were used for sampling the KT sequence since no single locality exposes a complete section (Fig. 1). Marker units (^{14}C dates from Swanson et al. 2012a) include the Basal Reticulite (~1500 C.E.), the Layer 6 Scoria (~1650 C.E.), the Circumferential Lava Flow (~1670–1700 C.E.), the Golden Pumice (between 1790 and 1820 C.E.), and the Eastern Pumice (younger than the Golden Pumice; Fig. 1c). The Golden Pumice and Eastern Pumice have different compositions and erupted from different parts of the caldera, and no pyroclastic deposit is known between them. The Circumferential Lava Flow is unusual because it erupted from a caldera boundary fault ~2.5 km south of the caldera (Fig. 1). Two pumice-rich layers found between the Basal Reticulite and the Layer 6 Scoria are from 1500 to 1650 C.E. (here called units 7 and 11), and one pumice-rich layer between the Layer 6 Scoria and the Circumferential Lava Flow is from ~1650 to 1670 C.E. (here called unit 20; Fig. 1c).

Tephra samples were cleaned, gently crushed, and sieved into 0.5–1.0 and 1.0–1.65 mm size fractions. Olivine is almost always the only phenocryst phase in these

Table 1 Keanakāko‘i Tephra samples examined in this study

Name	Age[a] (C.E.)	Sample type[a,b]
Eastern pumice[c]	~1790–1820	Pumice fall deposit
Golden pumice	~1790–1820	Pumice fall deposit
Circumferential flow (CLF)	~1670–1700	Lava flow, erupted SW of summit caldera
unit 20	~1650–1670	Lithic-bearing vitric ash, thinly bedded
Layer 6	~1650	Scoria fall
unit 11 unit 7	~1500–1650	Lithic-bearing vitric ash, thinly bedded, falls and fine surges
Basal Reticulite	~1500	Reticulite fall deposit

[a] Based on ^{14}C ages from Swanson et al. (2012a)

[b] Sharp et al. (1987)

[c] Since the publication of Swanson et al. (2012a), the Eastern Pumice has been found to overlie the Golden Pumice (Swanson et al. 2017)

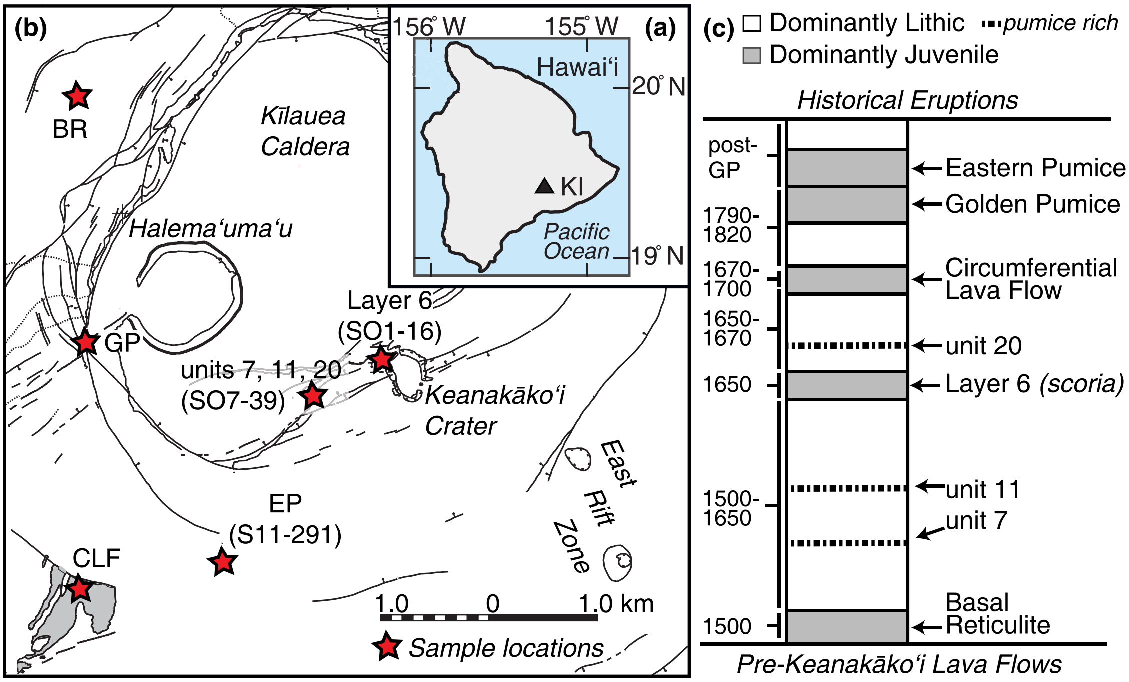

Fig. 1 **a** The Island of Hawai‘i, with black triangle identifying Kīlauea's summit. **b** Simplified summit map of Kīlauea Caldera with major faults and structural boundaries (modified after Neal and Lockwood 2003). *Red stars* indicate locations for the KT samples used in this study: Basal Reticulite (BR), units 7, 11, and 20 (SO7-39), Layer 6 (SO1-16), Circumferential Lava Flow (CLF; *filled in grey*), Eastern Pumice (EP; S11-291), and Golden Pumice (GP). **c** Simplified composite stratigraphic column (not to scale) for the Keanakāko‘i Tephra modified after Swanson et al. (2012a). Since that paper was published, Eastern Pumice has been found to overlie Golden Pumice (Swanson et al. 2017). Approximate ^{14}C ages are from Swanson et al. (2012a). *White* units are phreatomagmatic eruptions with dominantly lithic material, whereas *grey* denotes deposits of primarily juvenile material. *Dashed lines* show juvenile-rich phreatomagmatic units selected for this study. (For all references to color in figure captions, the reader is referred to the web version of this article.)

samples, and contains equant spinel inclusions (<0.1 mm). Olivine phenocrysts with obvious crystal faces (Fig. 2) and adhering glass were handpicked from both size fractions using a binocular microscope so that both crystal rim and glass compositions could be measured. Individual crystals were carefully mounted in epoxy in a 2.5-cm round plug to ensure that they were ground and polished perpendicular to a principal crystallographic axis down to the crystal core. This method minimized off-center and highly oblique sections, which can introduce significant error in diffusion timescale estimates (Shea et al. 2015a). Glassy samples from the Circumferential Lava Flow were made into standard polished thin sections.

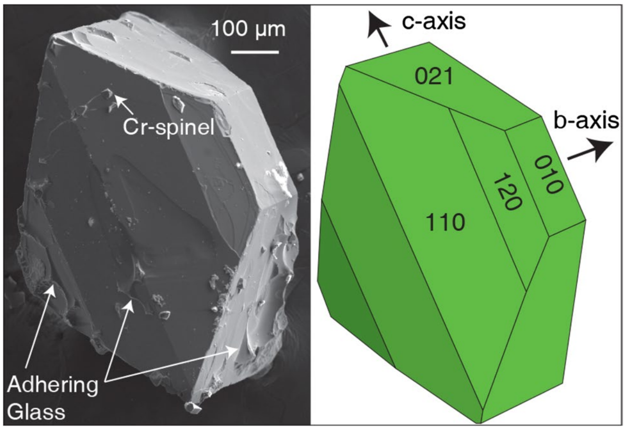

Fig. 2 Secondary electron image (SEI) of a typical euhedral olivine crystal observed in KT deposits (*left*). Adhering glass was removed from this crystal using a HF acid bath (see Supplementary Material) to document typical olivine morphology in KT deposits. Schematic (*right*) shows crystal faces and orientation of crystallographic axes in SEI image. These features allowed for careful orientation of individual crystals perpendicular to the *a*- or *b*-axes during sample preparation. Crystals were also carefully ground and polished to expose their cores, reducing modeling errors associated with off-center and highly oblique sections (Shea et al. 2015a)

Methods

Electron probe micro-analysis (EPMA)

Major and minor element analyses of olivine were made at the University of Hawai‘i (UH) and Nanyang Technological University (NTU) using JXA-8500F and JXA-8530F JEOL Hyperprobes, respectively. Crystals were catalogued by zoning type (e.g., normal, reverse, complex) using backscatter electron (BSE) images to define populations within each eruption. Cores (i.e., at the geometric center of the 2D olivine crystal section) from 424 olivine crystals were analyzed at UH using a 20 kV accelerating voltage and 10 μm beam with a 200 nA current. The same conditions with a 1 μm beam were used to measure profiles with 3–10 μm spacing across 62 olivine crystals with concentration gradients previously identified in BSE images (10–11 per sample for units 7, 11, and 20, Layer 6, and Golden and Eastern Pumices). BSE images allowed selection of olivine crystals with symmetric concentration gradients and clear grayscale plateaus at the cores. Each traverse was oriented perpendicular to a well-formed crystal face avoiding corners to minimize the effects of merging diffusion fronts (e.g., Shea et al. 2015a). Traverses were selected only for crystal faces with adhering glass to ensure the precise measurement of a crystal rim composition within 5 μm of the olivine–glass boundary. Peak counting times were 60 s for Si, Fe, Mg, Ca, and Ni, and backgrounds for all analyses were measured on each side of the peaks for 30 s. Standards were routinely measured every 2–3 h to monitor for instrumental drift. San Carlos olivine (USNM 111312/444; Jarosewich et al. 1980) was used for Si, Fe and Mg calibration, a synthetic nickel-oxide for Ni, and Kakanui Augite (USNM 122142; Jarosewich et al. 1980) for Ca. Two-sigma relative precision, based on repeated analyses of San Carlos olivine, are 0.26 wt% for SiO_2, 0.32 wt% for MgO, 0.06 wt% for FeO, 0.002 wt% for NiO, and 0.001 wt% for CaO (see Supplementary Material).

Additional core-rim zoning profiles were measured at NTU for olivine crystals from the Basal Reticulite ($n = 11$) and the Circumferential Lava Flow ($n = 8$), yielding a total of 81 profiles from unique crystals for this study. Analytical conditions were a 15-kV accelerating voltage and 40-nA current with a focused beam and 2–3 μm spacing. Peak counting times were 20 s for Si, Mg, and Fe, 60 s for Mn, and 90 s for Ni and Ca. The mean atomic number background intensity data were calibrated and continuum absorption corrected for Si ka, Mg ka, Fe ka, Mn ka, Ni ka, and Ca ka (Donovan and Tingle 1996). Astimex reference standards for analyses were olivine (#134) for Si, Fe, Mg, and Ni, rhodonite (#139) for Mn, and diopside (#121) for Ca. Two-sigma relative precision for analyses are within 0.68 wt% for SiO_2, 0.38 wt% for MgO, 0.15 wt% for FeO, and 0.008 wt% for NiO, MnO, and CaO. Repeat measurements of olivine core compositions at both UH and NTU produced comparable results within the relative precision determined from standard analyses. For all measurements, X-ray intensities were converted to concentrations using standard ZAF corrections (Armstrong 1988). Analyses with totals <99.0 and >100.5 wt% and/or cation totals <2.98 or >3.02 were rejected.

Electron backscatter diffraction (EBSD)

The orientation of the crystallographic axes in olivine crystals are necessary to correct for diffusion anisotropy (e.g., Costa and Chakraborty 2004). Crystal orientations for all 81 olivine sections were determined using a HKL Nordlys EBSD detector on a JEOL JSM-5900LV scanning electron microscope at UH. Additional polishing with a 50–70 nm colloidal silica suspension for 4 h on a vibratory polisher improved the quality of electron backscatter diffraction patterns (EBSPs). Measurements were taken using a 70° sample tilt, 25-kV accelerating voltage, and a minimized working distance (generally 12–15 mm). Grids of 10 × 10 points spaced at least 10 μm apart achieved mean angular deviation values of <1°. The EBSPs were processed using the HKL Technology Channel 5 software package, and axis locations were output into lower hemisphere stereographic projections (see Prior et al. 1999 for EBSD technique details). Crystallographic orientation was the same within individual grains over areas of 100–1000 μm^2, consistent with a juvenile magmatic origin for the phenocrysts (e.g., antecrysts are commonly deformed; Helz 1987; Clague and Denlinger 1994).

The angles α, β, and γ between the measured electron probe traverse and the crystallographic *a*-, *b*-, and *c*-axes, respectively (Costa and Chakraborty 2004), were calculated using Stereonet 9© (Cardozo and Allmendinger 2013).

Diffusion modeling

The olivine compositional profiles in this study are interpreted to result from diffusive re-equilibration. This was tested by comparing the compositional profiles along different crystallographic directions. Given that the diffusion coefficient of Fo and Ni are six times larger along [001] than along [100] and [010] (Dohmen and Chakraborty 2007a), concentration distances should be proportional to the different diffusivities along different directions. We tested several crystals and found that the diffusion distances were at least 2× wider in profiles parallel to the *c*-axis compared to profiles roughly parallel to the *a*- or *b*-axes (see Supplementary Material). This demonstrates that the width of the compositional profiles are broadly proportional to the diffusion coefficient, consistent with the factor of 2.4 found in ideal sections from numerical models in Shea et al. (2015a). These observations indicate that most of the Fe–Mg profile is controlled by diffusion and not growth.

Geochemical profiles of Fe–Mg and Ni from EPMA traverses were modeled using the program DIPRA (Girona and Costa 2013), which numerically solves the one-dimensional concentration-dependent diffusion equation to obtain timescales. The program incorporates diffusion coefficients for Fe–Mg from Dohmen and Chakraborty (2007a, b) and Ni from Petry et al. (2004). Anisotropy-corrected diffusivities were calculated by DIPRA for each traverse based on the angles between the analytical profile and the *a*-, *b*-, and *c*-axes measured by EBSD (α, β, and γ, respectively; Costa and Chakraborty 2004). The initial condition (C_i) was determined based on the compositions of well-defined core concentration plateaus and the boundary condition (C_o) was the melt Mg# in Fe–Mg equilibrium (Matzen et al. 2011) with the measured Fo content of each olivine rim or inferred rim in complex zoning patterns (e.g., minimum of hook zoning, maximum of shoulder zoning). DIPRA models provided best-fit results and timescale errors that are based on estimated analytical precision and uncertainty in temperature for a chosen thermometer (Girona and Costa 2013).

The intrinsic properties required as inputs in DIPRA (e.g., *T*, *P*, f_{O_2}) are well known for Kīlauea magmas. Temperature was calculated using the Kīlauea MgO thermometer (Helz and Thornber 1987) and the inferred melt MgO (6.2–14.6 wt%) from each individual olivine rim boundary condition (C_o). These values ranged from 1139 to 1307 °C (±10°C; Helz and Thornber 1987) and are akin to the magma temperature for storage and diffusion recorded by each crystal. Oxygen fugacity conditions (~QFM) were chosen based on the range of f_{O_2} found by Moussallam et al. (2016), Helz et al. (2017) and Davis et al. (2017) for Kīlauea olivine-hosted melt inclusions and Hawaiian xenoliths. Additional models were run at QFM + 0.4 log units (Helz et al. 2017) to characterize the effects of more oxidizing conditions proposed for undegassed magmas at depth. We used a pressure of 85 MPa, which approximates the depth of the modern South Caldera reservoir (~3.5 km; Cervelli and Miklius 2003; Poland et al. 2014) and provides one possible crustal storage depth for magmas during the KT period.

Results

Olivine cores with primitive compositions ($\geq Fo_{88}$) were found in all of the KT samples (Fig. 3, see also Table 2 and Supplementary Material). Early KT units (Basal Reticulite, units 7 and 11; 1500–1650 C.E.) also have heterogeneous olivine core Fo contents (e.g., 80–90) with diverse population distributions (Fig. 3). Olivine cores from ~1650 to 1670 C.E. (Layer 6 and unit 20) show bimodal distributions with $\geq Fo_{88}$ and intermediate compositions (Fo_{82-85}; Fig. 3). The two populations can also be discriminated by their morphologies. Olivine crystals with $\geq Fo_{88}$ are typically larger (>0.5 mm across), euhedral, and lack Cr-spinel and melt inclusions (Fig. 4a). In contrast, Fo_{82-85} olivine crystals are usually smaller (0.1–0.5 mm across) and have skeletal morphologies with abundant Cr-spinel and melt inclusions (Fig. 4b). The Fo distribution for Layer 6 is strongly bimodal, with a pronounced high-Fo peak, and a broad intermediate mode (Fig. 3). The primitive Fo mode in unit 20 is wider and the distribution has a smaller, secondary intermediate peak. Olivine core compositions late in the KT (Circumferential Lava Flow, Golden Pumice, Eastern Pumice; ~1670–1820 C.E.) have broad distributions of primitive to intermediate populations (Fo_{83-90}; Fig. 3). The Circumferential Lava Flow is unusual in that it also has a population of evolved ($<Fo_{80}$) olivine core compositions.

The core-to-rim transects for all 81 olivine crystals highlight the diversity of zoning patterns. Forsterite profiles are subdivided into four types, and NiO zoning typically mimics Fo zoning. Most olivine crystals have normal zoning ($Fo_{core} > Fo_{rim}$; Fig. 5a) with primitive core plateaus ($\geq Fo_{88}$) that decrease 1–5 mol% Fo towards the rim. Reversely zoned olivine crystals ($Fo_{core} < Fo_{rim}$; Fig. 5b) have low-Fo cores (e.g., 82) and are relatively rare in KT deposits. These crystals typically have a 1–6 mol% change in Fo between the core and the rim. 'Complex' zoning patterns are classified as: (1) hook (Fig. 5c), which are mostly normally zoned but have 5–20 µm reversely zoned rims, and (2) shoulder (Fig. 5d), which are mostly reversely zoned with 5–20 µm of normal zoning at the rim. These compositional reversals in complexly zoned olivine crystals indicate that more than

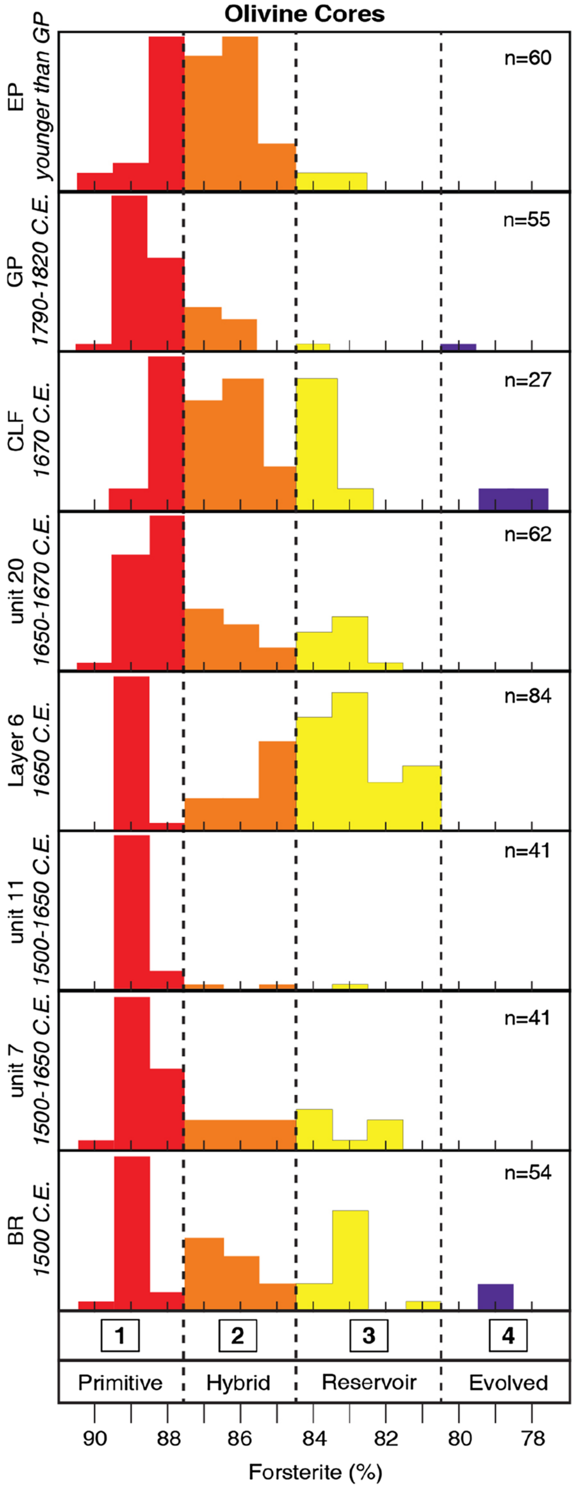

Fig. 3 Histograms of core Fo contents for KT olivine populations. Panels are listed in stratigraphic order from the oldest at the bottom. Bins span a 1 mol% range of Fo. All histograms are normalized to 1 (no *y*-axis scale) to allow direct comparison. *Boxed numbers* on *x*-axis (1–4) denote olivine populations within each eruption in order of decreasing Fo content

one mixing event is recorded. Hook profiles generally have steep normal zoning from primitive Fo_{88} to $<Fo_{80}$ (Fig. 5c), reflecting initial mixing of primitive magmas with a low-Mg# melt. Hook and shoulder profiles do not always preserve compositional reversals in NiO (e.g., Fig. 5c). Calcium was not significantly zoned in most KT olivine crystals, with minor compositional changes occurring only in the outer 5–20 µm rims. Thus, Ca was not modeled for timescale information and is not discussed further.

Diffusion timescales obtained from modeling 123 Fe–Mg and NiO profiles in KT olivine crystals vary from a few days to about 2 years (Table 3). Timescales for hook and shoulder profiles were obtained only for the larger zoned interior regions of the profiles (red lines in Fig. 5c, d), not the outermost thin rims (blue dashed lines). The calculated errors from DIPRA, based on analytical precision (±0.1 mol% for Fo and ±0.008 wt% for NiO) and temperature uncertainty (±10 °C; Helz and Thornber), are on average ±33% for Fo and ±47% for NiO relative to the timescale calculated for each olivine profile (Table 3). If diffusion occurred under conditions more oxidizing than QFM (e.g., QFM + 0.4 log units; Helz et al. 2017) the modeled timescales would be on average 20% shorter than the values reported here (e.g., 25 days vs. 31 days). Additionally, the temperatures used for diffusion models may be too high, as the Helz and Thornber (1987) thermometer was calibrated for 1 atm and low water content. Thus, calculated timescales in this study may represent minimum storage durations. The diffusion timescales do not systematically correlate with zoning type, core Fo content, or stratigraphic order.

For the 55 crystals where Fo and Ni could both be modeled, about half have Ni timescales that are shorter than Fo and do not agree within error (Table 3). Discrepancies between Fo and Ni timescales were previously noted by Costa and Dungan (2005). The slopes of Fe–Mg and Ni on logD vs. $10^4/T$ plots are not parallel (e.g., Chakraborty 2010 and references therein). This results in an increasing mismatch between Fo and Ni diffusion coefficients with decreasing temperature (Costa and Dungan 2005), but could also reflect that the diffusion coefficient of Ni is less well characterized than Fo. Furthermore, the analytical error relative to the change in concentration for each component contributes to the calculated error and potentially the degree of discrepancy. For example, the analytical precision of Fo (±0.1 mol%) is 2% of a profile with 6 mol% Fo zoning, whereas the Ni precision (±0.008 wt%) is 8% of a profile with 0.10 wt% NiO zoning. Although Fo timescales are preferred in diffusion studies (e.g., Kahl et al. 2011, 2013; Albert et al. 2015; Hartley et al. 2016), many KT olivine show good agreement between Fo and Ni. Here, we provide both Fo and Ni timescales for comparison.

Table 2 Representative olivine core and rim compositions for dominant modes in individual eruption populations (e.g., Fig. 3)

Oxide (wt%)	Basal Reticulite		unit 7		unit 11		Layer 6 (mode 1)	
	Core	Rim	Core	Rim	Core	Rim	Core	Rim
SiO_2	39.7	39.1	40.2	40.0	40.3	40.3	40.3	39.9
FeO	10.6	12.7	10.8	12.1	10.9	12.8	10.7	12.2
MgO	48.8	46.6	48.7	47.5	48.2	46.1	48.6	46.8
NiO	0.47	0.39	0.46	0.41	0.48	0.37	0.45	0.40
CaO	0.20	0.22	0.20	0.22	0.20	0.24	0.19	0.23
Total	99.8	99.0	100.4	100.2	100.1	99.8	100.2	99.5
Fo (%)[a]	89.1	86.8	89.0	87.5	88.7	86.5	89.0	87.2
Oxide (wt%)	Layer 6 (mode 2)		unit 20 (mode 1)		unit 20 (mode 2)		CLF (mode 1)	
	Core	Rim	Core	Rim	Core	Rim	Core	Rim
SiO_2	38.9	39.1	39.4	41.2	40.3	40.5	40.6	39.2
FeO	15.8	16.6	11.2	11.8	15.9	14.1	12.4	35.7
MgO	44.4	43.6	47.9	46.4	43.7	45.3	46.1	24.2
NiO	0.24	0.22	0.42	0.40	0.30	0.29	0.36	0.20
CaO	0.22	0.24	0.19	0.22	0.19	0.25	0.19	0.25
Total	99.6	99.8	99.1	100.0	100.4	100.4	99.7	99.5
Fo (%)	83.4	82.4	88.4	87.5	83.0	85.1	86.9	77.3
Oxide (wt%)	CLF (mode 2)		CLF (evolved)		Eastern Pumice		Golden Pumice	
	Core	Rim	Core	Rim	Rim	Core	Core	Rim
SiO_2	40.3	39.6	39.3	39.1	39.7	40.3	39.6	39.7
FeO	15.0	18.7	20.0	21.1	11.9	15.0	18.7	11.9
MgO	44.0	41.2	39.9	39.2	47.9	44.3	40.3	47.9
NiO	0.26	0.22	0.21	0.18	0.37	0.26	0.21	0.37
CaO	0.19	0.21	0.24	0.24	0.24	0.19	0.24	0.24
Total	99.8	99.9	99.7	99.8	100.1	100.1	99.1	100.1
Fo (%)	84.0	79.7	78.6	77.5	87.8	84.0	79.3	87.8

Two modes are reported for bimodal distributions. Full dataset can be found in the Supplementary Material

[a] Fo, forsterite = [Mg/(Mg + Fe) × 100]

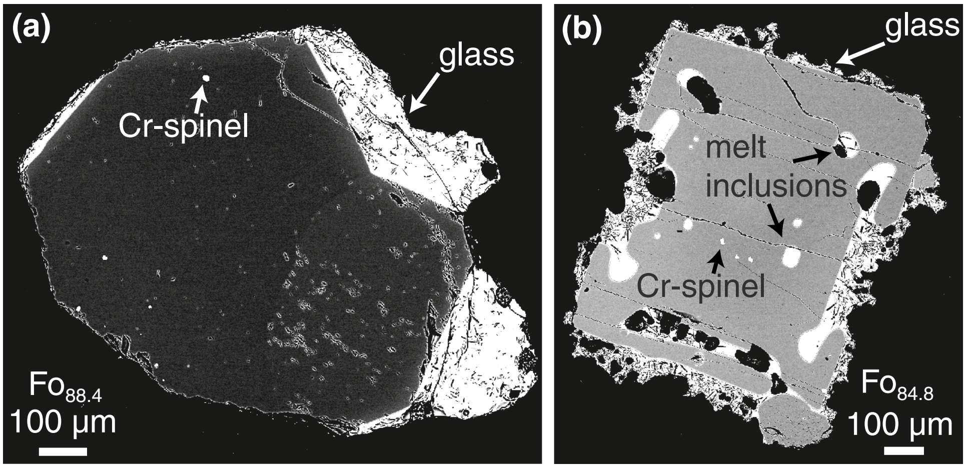

Fig. 4 Backscatter electron (BSE) images highlighting textural differences between olivine crystals from the **a** primitive ($\geq Fo_{88}$; grey marks on olivine are pits from polishing) and **b** reservoir (e.g., $Fo_{80–85}$) populations from the histograms shown in Fig. 3. The primitive olivine crystals generally have well-formed faces and rare Cr-spinel or melt inclusions. The lower-Fo olivine crystals typically have skeletal morphologies with abundant Cr-spinel and melt inclusions

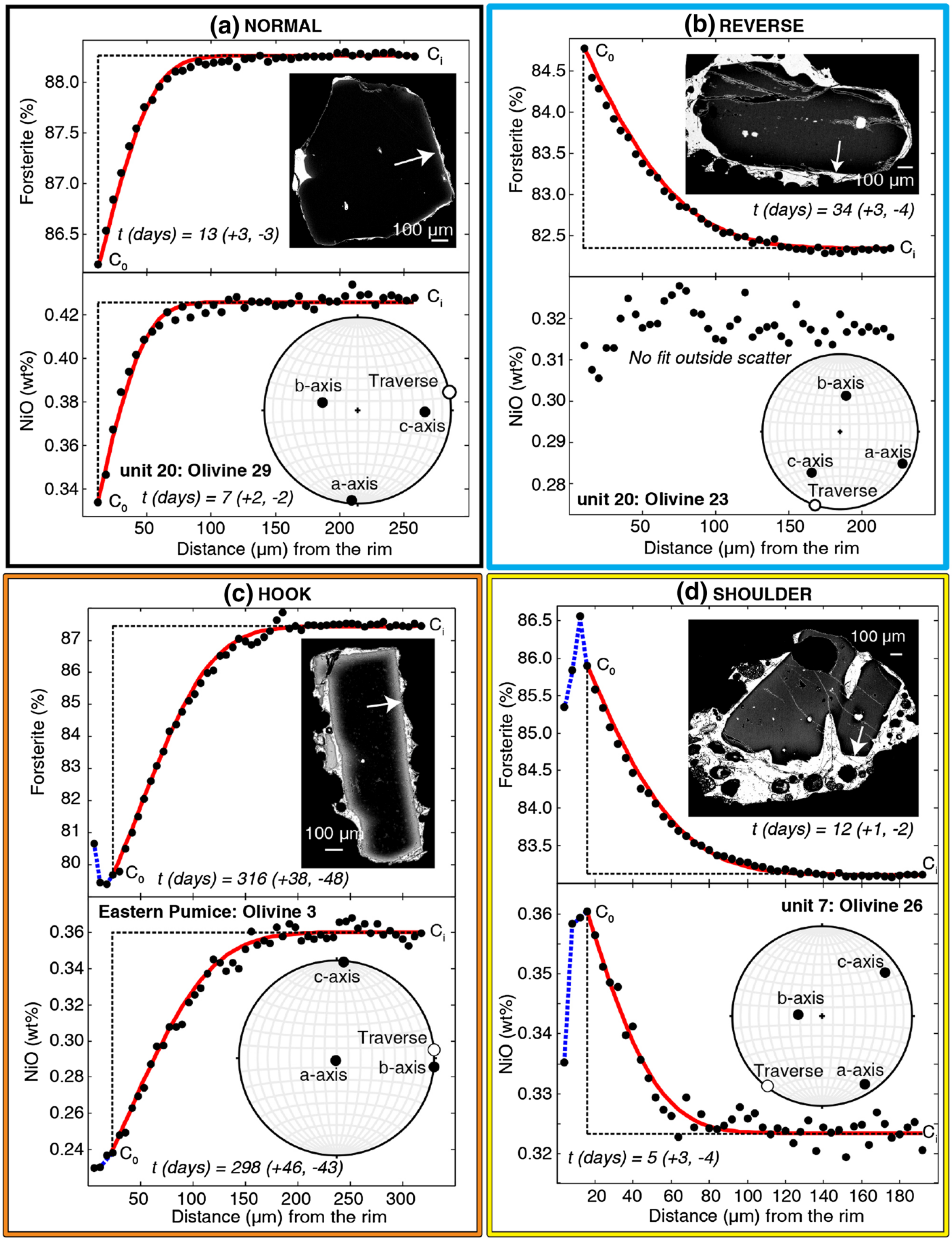

Fig. 5 Olivine zoning profiles (rim on left). Profile types are: **a** normal (*black box*), **b** reverse (*blue box*), **c** hook (*orange box*), or **d** shoulder (*yellow box*) based on the change in concentration between the core and the rim. *Colored boxes* around zoning types are consistent with zoning patterns as presented in Fig. 9. BSE images and lower hemisphere projections illustrate the location of the analytical traverse and orientation of the crystallographic axes. *Red lines* show best-fit results from diffusion models with calculated timescales (Table 3). *Blue dashed lines* in hook and shoulder profiles highlight an additional mixing event followed by limited diffusive re-equilibration that cannot be easily fit by diffusion models

Table 3 Calculated times (days) obtained by modeling the chemical diffusion of Fe–Mg and Ni in olivine crystals

Sample	Ol.	*T* (°C)	*α*	*β*	*γ*	Elem.	C_i	C_o	*t* (days)	Δ (−)	Δ (+)
BR	5	1307	44	86	46	Fo	88.7	86.8	0.6	0.4	0.2
						Ni	0.443	0.400	0.5	0.2	0.3
	7	1245	32	59	88	Fo	82.0	82.3	3.1	3.4	206
						Ni	0.295	0.275	13	10	7
	9	1307	88	60	30	Fo	91.1	90.1	38	10	10
						Ni	0.450	0.423	9	1	1
	12	1307	89	31	57	Fo	86.9	88.2	73	9	8
						Ni	0.395	0.425	18	4	5
	15	1307	16	79	78	Fo	88.8	84	0.2	0.2	0.4
						Ni	0.440	0.290	0.2	0.3	0.1
	16	1245	86	64	26	Fo	86.9	84.8	46	11	6
						Ni	0.4	0.34	35	5	12
	17	1307	18	73	89	Fo	88.2	88.7	209	22	24
						Ni	0.425	0.444	6	4	1
	21	1245	82	17	72	Fo	88.5	88.0	467	56	86
						Ni	0.438	0.415	163	34	32
	28	1245	82	8	83	Fo	78.0	83.5	78	16	16
						Ni	0.270	0.300	31	7	4
U7	1	1281	17	80	77	Fo	89.0	87.0	10	4	3
						Ni	0.457	0.408	8	6	2
	8	1281	5	87	87	Fo	84.4	86.2	10	3	4
						Ni	0.297	0.341	2	1	1
	12	1281	19	72	89	Fo	88.3	87.1	41	18	15
						Ni	0.417	0.387	17	14	14
	14	1245	70	21	82	Fo	86.2	87.5	295	40	60
						Ni	0.350	0.375	58	46	24
	17	1245	65	26	83	Fo	86.2	84.7	634	93	96
						Ni	0.332	0.316	401	353	781
	20	1281	56	40	74	Fo	89.3	86.9	42	5	6
						Ni	0.463	0.377	7	3	2
	26	1281	85	74	16	Fo	83.1	85.8	12	1	2
						Ni	0.323	0.36	5	3	4
	28	1281	72	64	32	Fo	89.4	87.6	4	1	0.5
						Ni	0.460	0.406	2	2	1
	29	1281	77	16	81	Fo	88.3	87.0	190	60	58
						Ni	0.418	0.380	65	29	33
U11	4	1275	23	72	78	Fo	83.7	82.9	434	201	69
						Ni	0.297	0.263	60	11	32
	6	1291	21	68	84	Fo	88.7	89.4	149	60	99
						Ni	0.450	0.460	39	39	262
	7	1291	78	32	61	Fo	88.4	86.9	97	20	27
						Ni	0.389	0.344	145	9	8
	9	1291	33	59	75	Fo	89.7	88.2	30	7	5
						Ni	0.436	0.355	17	4	2
	14	1291	75	59	35	Fo	88.7	89.27	2	1.5	1
						Ni	–	–	–	–	–
	19	1291	47	41	85	Fo	89.5	89.2	37	31	43
						Ni	–	–	–	–	–
	25	1291	56	78	89	Fo	88.9	89.4	444	261	459
						Ni	–	–	–	–	–
	34	1291	43	84	47	Fo	88.6	89.3	197	82	286

Table 3 (continued)

Sample	Ol.	T (°C)	α	β	γ	Elem.	C_i	C_o	t (days)	Δ (−)	Δ (+)
						Ni	–	–	–	–	–
L6	4	1197	77	56	37	Fo	85.2	81.3	443	50	56
						Ni	0.332	0.210	361	45	57
	6	1197	85	21	68	Fo	84.6	84.5	831	129	153
						Ni	0.272	0.212	190	52	34
	8	1263	46	44	88	Fo	81.6	82.7	11	3	4
						Ni	–	–	–	–	–
	20	1263	86	90	4	Fo	89.1	87.9	93	17	18
						Ni	0.457	0.415	61	7	10
	24	1197	90	1	89	Fo	88.0	81.2	708	79	94
						Ni	0.433	0.210	421	58	58
	30	1263	9	84	81	Fo	88.7	84.5	3	3	2
						Ni	0.457	0.270	3	3	1
	34	1263	8	83	87	Fo	89.2	87.5	66	26	26
						Ni	0.473	0.425	37	9	14
U20	9	1275	34	58	77	Fo	83.7	84.6	56	18	15
						Ni	–	–	–	–	–
	17	1275	86	88	5	Fo	86.5	85.2	50	17	15
						Ni	0.391	0.323	26	5	5
	18	1275	29	69	70	Fo	86.5	87.6	16	4	4
						Ni	0.323	0.340	1	1	1
	23	1275	82	52	39	Fo	82.3	84.7	34	3	4
						Ni	–	–	–	–	–
	29	1275	75	61	31	Fo	88.3	86.2	13	3	3
						Ni	0.427	0.335	7	2	2
	34	1275	42	81	49	Fo	87.9	88.3	189	11	120
						Ni	0.390	0.420	230	44	32
	35	1275	34	60	75	Fo	83.8	84.6	75	13	20
						Ni	–	–	–	–	–
	36	1275	88	10	81	Fo	87.9	86.9	243	33	58
						Ni	–	–	–	–	–
CLF	14_18	1180	22	71	82	Fo	78.8	80.0	129	18	24
						Ni	0.195	0.230	63	20	12
	14_21	1139	77	15	86	Fo	77.7	79.2	490	72	70
						Ni	0.185	0.220	167	39	43
	14_22	1188	35	56	85	Fo	87.0	77.3	67	11	11
						Ni	0.370	0.200	49	7	9
	16_9	1189	29	85	61	Fo	83.3	84.8	17	8	8
						Ni	0.195	0.175	47	11	10
	16_11	1188	37	63	68	Fo	84.0	84.9	9	5	11
						Ni	–	–	–	–	–
	16_3	1139	73	14	87	Fo	85.6	81.5	6	5	1
						Ni	–	–	–	–	–
	16_7	1188	72	57	38	Fo	84.0	84.9	12	2	2
						Ni	–	–	–	–	–
GP	6	1275	31	90	59	Fo	88.5	89.1	226	115	93
						Ni	0.428	0.441	115	106	315
	12	1237	78	65	28	Fo	89.3	83.4	20	5	5
						Ni	0.450	0.252	12	2	2
	20	1275	41	71	87	Fo	88.9	86.5	193	39	44
						Ni	0.438	0.360	30	7	4

Table 3 (continued)

Sample	Ol.	T (°C)	α	β	γ	Elem.	C_i	C_o	t (days)	Δ (−)	Δ (+)
	22	1275	28	70	71	Fo	88.3	86.0	209	29	36
						Ni	0.432	0.320	114	21	15
	23	1275	43	75	50	Fo	86.8	88.1	14	6	16
						Ni	0.390	0.420	10	5	19
	27	1275	89	16	75	Fo	88.4	86.3	385	88	89
						Ni	0.43	0.31	60	8	18
	30	1275	79	64	26	Fo	88.3	86.0	257	40	46
						Ni	0.435	0.340	163	37	24
	31	1275	55	81	36	Fo	88.7	86.1	121	13	13
						Ni	0.413	0.350	24	7	11
	32	1237	26	78	66	Fo	88.2	79.7	427	48	57
						Ni	0.410	0.275	101	13	17
	34	1237	29	60	83	Fo	88.5	81.7	217	41	32
						Ni	0.425	0.325	54	9	13
	36	1275	28	66	80	Fo	85.1	86.2	67	26	44
						Ni	0.285	0.325	66	29	15
EP	3	1237	81	10	89	Fo	87.5	79.9	316	38	48
						Ni	0.360	0.245	298	46	43
	5	1275	85	84	7	Fo	87.1	87.7	26	9	6
						Ni	0.370	0.388	34	10	109
	6	1237	80	58	34	Fo	87.1	85.8	4	3	1
						Ni	0.360	0.335	2	2	2
	13	1237	84	63	27	Fo	86.5	87.2	524	116	229
						Ni	0.335	0.355	321	183	40
	15	1237	81	48	44	Fo	87.7	81.4	91	12	11
						Ni	0.365	0.255	0.89	0.19	0.17
	19	1237	61	34	73	Fo	87.8	81.5	31	8	7
						Ni	0.377	0.310	17	8	7
	23	1237	90	74	15	Fo	83.3	84.6	49	6	7
						Ni	–	–	–	–	–
	27	1237	83	77	14	Fo	87.3	82.8	85	10	10
						Ni	0.350	0.240	51	8	8
	30	1237	18	73	88	Fo	87.3	86.5	49	29	19
						Ni	0.355	0.330	14	15	23

Sample abbreviations are the same as in Fig. 1. All olivine profiles were modeled using P = 85 MPa and f_{O_2} = QFM. The angles between the analytical traverse and the *a*-, *b*-, and *c*-axes are reported as α, β, and γ, respectively (Costa and Chakraborty 2004). C_i is the initial condition (e.g., olivine core concentration plateau) and C_o is the boundary condition (e.g., olivine rim composition). Δ(−) and Δ(+) are the errors on the time calculated by DIPRA (Girona and Costa 2013) after the anisotropy correction. They account for temperature uncertainties (±10 °C) and model fit within analytical uncertainty (Fo = ± 0.1 mol%; Ni = ± 0.008 wt%). A dash represents zoning profiles for which no timescales could be calculated due to small changes in concentration

Most (65%) calculated timescales record less than 3 months of storage and diffusive re-equilibration (Fig. 6a). The shorter range of the timescales record mixing and subsequent storage on the order of 1–3 weeks (45%; Fig. 6b). These profiles and calculated timescales demonstrate that KT magmas were mixed and stored for significant durations at magmatic temperatures before eruption, contrary to previous interpretations of little to no storage during rapid ascent from the mantle (e.g., Sides et al. 2014). Compositional reversals in hook and shoulder profiles (blue lines; Fig. 5c, d) have limited spatial resolution (defined by 3–6 points), a small change element concentration (~1% for Fo, <0.03 wt% for NiO), and many are only recorded by Fo and not NiO. These zoning features cannot be fit with adequate precision using diffusion models. Thus, no timescales were retrieved for this additional, late-stage mixing event.

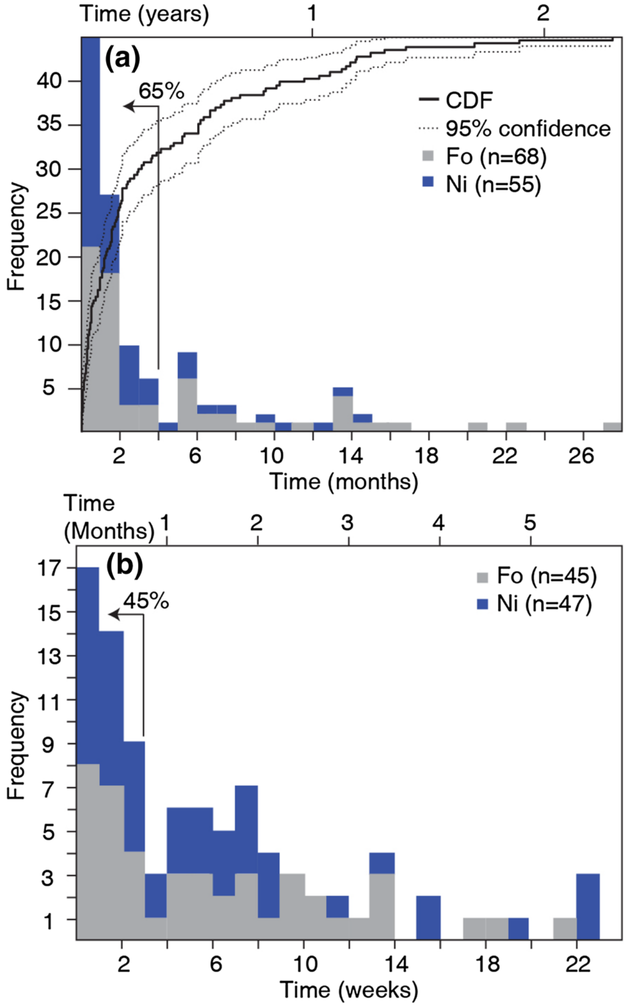

Fig. 6 Histograms showing the range and frequency of timescales retrieved from modeling Fo ($n = 68$) and NiO ($n = 55$) profiles in KT olivine crystals. *Solid black line* is the cumulative distribution function (CDF) of the full dataset with 95% confidence intervals (*dotted lines*). **a** Bins represent 1 month. 65% of the timescales are less than 2 months in duration. **b** Bins represent 1 week for timescales from 0 to 6 months. 45% of the timescales are less than 3 weeks in duration

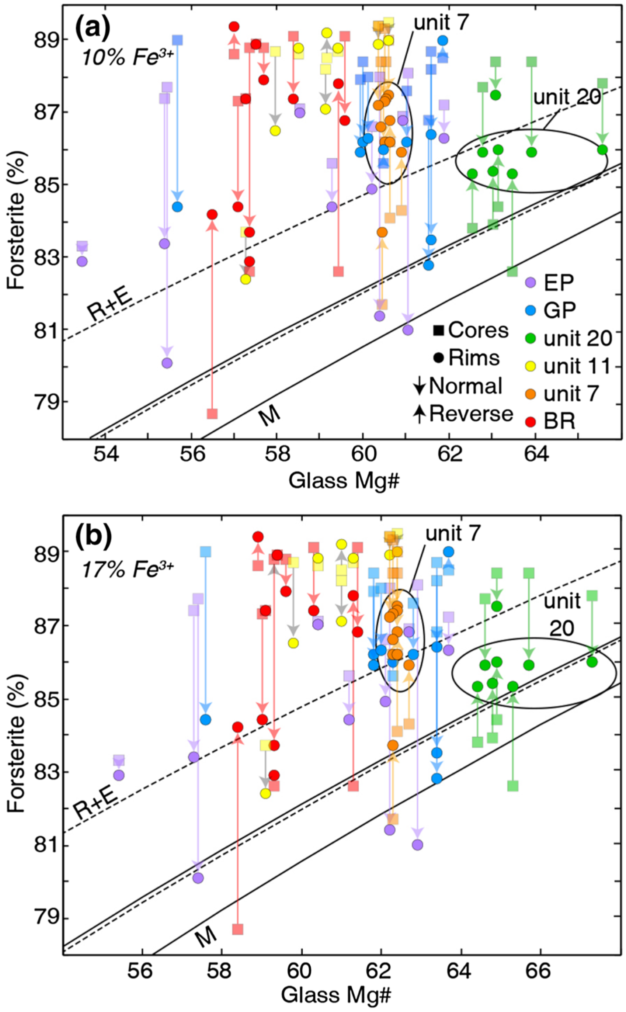

Fig. 7 Glass Mg-numbers [Mg# = Mg/(Mg + Fe^{2+}) × 100] plotted against KT olivine core (*squares*) and rim (*circles*) forsterite contents (no data for Layer 6 or Circumferential Lava Flow are included due to microlite-rich matrix). *Arrows* point in the direction of zoning toward the olivine rim (e.g., down denotes normal zoning, up denotes reverse zoning). The *solid lines mark* the shallow pressure (1 atm) equilibrium field ("M", Fe–Mg $K_D = 0.343 \pm 0.008$) of Matzen et al. (2011), whereas dashed lines ("R + E", Fe–Mg $K_D = 0.30 \pm 0.03$) are from Roeder and Emslie (1970). **a** Mg# is calculated assuming $Fe^{3+}/Fe^T = 0.10$, based on iron titration f_{O_2} measurements for rapidly quenched, near vent Kīlauea glasses (Rhodes and Vollinger 2005). **b** Mg# is calculated assuming $Fe^{3+}/Fe^T = 0.17$ based on recent μ-XANES analyses of undegassed Kīlauea olivine-hosted melt inclusions (Helz et al. 2017). In both cases, most olivine cores and rims plot above the equilibrium field and represent non-equilibrium compositions. Samples with bimodal core populations (*circled data*; units 7 and 20) can be zoned toward similar rim compositions that are out of Fe–Mg equilibrium with the melts that carried the olivine crystals to the surface (e.g., unit 7)

Olivine rims within 5 μm of the crystal–melt boundary generally have Fo values that are too high to be in Fe–Mg equilibrium with their nearby (>20 μm distant to avoid boundary layers next to the crystal; Shea et al. 2015b) adhering glass Mg-number (Mg# = [Mg/(Mg + Fe^{2+}) × 100]; see Supplementary Material for glass analyses). The Mg# was calculated assuming $Fe^{3+}/Fe^T = 0.10$ and 0.17 based on a range of conditions from rapidly quenched and degassed (Fig. 7a; Rhodes and Vollinger 2005) to undegassed at depth (Fig. 7b; Helz et al. 2017). The units 7 and 20 have a bimodal population of olivine cores with convergent zoning (i.e., that are zoned toward unique intermediate rim compositions), providing clear evidence for diffusive re-equilibration within a hybrid melt composition after mixing. Fe–Mg disequilibrium between olivine rims and adhering glasses, including rims from unit 7 (which shows systematic zoning), suggest that the olivine crystals record limited diffusive re-equilibration within the melt(s) that carried them to the surface. Most eruptions have a wide range of glass Mg#s (e.g., Basal Reticulite, Fig. 7). This is consistent with variable MgO observed by Mucek (2012) and Helz et al. (2014, 2015) within single layers in the KT deposits, and has been interpreted to reflect late-stage magma mixing.

Discussion

The diversity and complexity of olivine populations and their zoning patterns are evaluated below to better understand the mixing and storage histories of magma that fed the KT eruptions. The compositions of olivine cores are used to infer the magmatic environment in which they grew (e.g., primitive vs. relatively evolved melts), whereas olivine zoning patterns and rim compositions are used here to characterize the magmatic environment(s) in which they resided prior to eruption (e.g., Kahl et al. 2011, 2013). The olivine population, zoning pattern, and rim composition data are combined with timescale information to provide a new perspective on mixing histories, storage timescales, and magma ascent for the KT period. These interpretations are used to propose a new model for Kīlauea's prehistoric magmatic plumbing system following the collapse of the summit caldera circa 1500 C.E.

Depths of olivine crystallization and storage

Recent studies have invoked ascent of olivine-bearing magmas from depths of >40 km under Kīlauea (Sides et al. 2014; Rae et al. 2016). However, experimental studies on primitive Kīlauea compositions (16 wt% MgO) have found that orthopyroxene is the stable liquidus phase at mantle depths (Eggins 1991; Wagner and Grove 1998). Rhyolite-MELTS (Gualda et al. 2012; Ghiorso and Gualda 2015) was used here to better understand the maximum depth that Kīlauea primitive magmas might form olivine, and therefore, record magma mixing histories and storage timescales. The P–T conditions for crystallization of primitive (≥Fo_{88}) KT olivine were modeled using a 15 wt% MgO glass with 0.4 wt% H_2O (the most MgO-rich glass known from Kīlauea; Clague et al. 1995; Table 4) with oxygen fugacities (f_{O_2}) at and just above the quartz–fayalite–magnetite oxygen reaction buffer (between QFM and QFM + 1). These f_{O_2} values cover the range of redox conditions proposed for Hawaiian magmas at depth (Helz et al. 2017; Davis et al. 2017). This starting composition was selected because it is in Fe–Mg equilibrium with $Fo_{89–90}$ olivine over the range of f_{O_2} considered, similar to the dominantly primitive modes found in KT deposits (~40% of all KT olivine are ≥Fo_{88}; Fig. 3).

Liquidus olivine with $Fo_{89–90}$ composition crystallizes at maximum temperatures ~1375–1390 °C and pressures 0.39–0.48 GPa over the range of f_{O_2} considered (Fig. 8). Olivine is not stable above 0.48 GPa and is replaced by orthopyroxene as the liquidus phase, consistent with previous experimental work on Hawaiian tholeiites (e.g., Eggins

Table 4 High-MgO Kīlauea glass composition used in MELTS modeling

Oxide (wt%)	57-7A[a]
SiO_2	48.9
Al_2O_3	10.8
FeO	11.2
MgO	15.0
CaO	8.91
Na_2O	1.71
K_2O	0.31
P_2O_5	0.18
TiO_2	1.96
H_2O	0.397
Total	99.1

[a] Sample 57-7A is a submarine glass grain from Kīlauea's Puna Ridge (Clague et al. 1995)

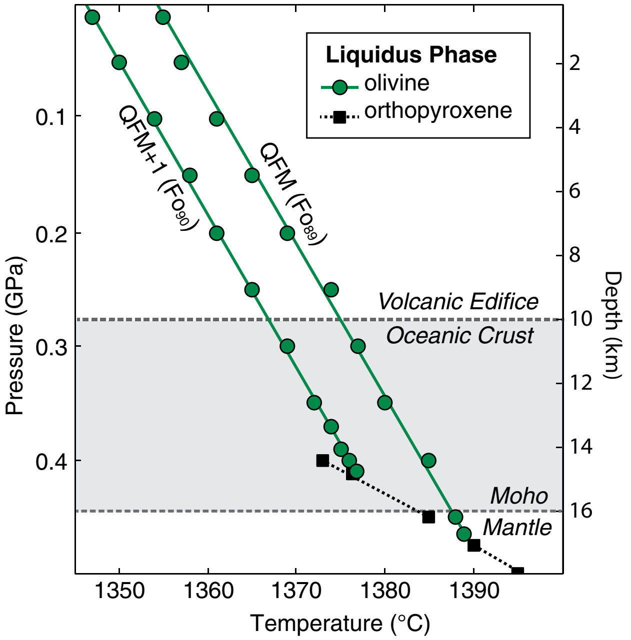

Fig. 8 MELTS-derived phase diagram identifying liquidus phases for crystallization of a 15 wt% MgO glass composition with 0.4 wt% H_2O (Clague et al. 1995; Table 4) at QFM (Moussallam et al. 2016; Helz et al. 2017; Davis et al. 2017) and QFM + 1 (Davis et al. 2017). Nodes represent pressures where MELTS models were run to determine the liquidus phase and its formation temperature. Depth–pressure equivalents were calculated assuming a density of 2.3 g/cm^3 for the first 1 km, and 2.9 g/cm^3 for depths >1 km. The resulting geostatic gradient is ~28 MPa/km for Kīlauea's crustal edifice. The boundary between Kīlauea and the oceanic crust is from Cayol et al. (2000) and Montgomery-Brown et al. (2015), whereas the base of the oceanic crust (Moho) is from Hill and Zucca (1987)

1991; Wagner and Grove 1998). The corresponding crystallization depths are ~15–17 km, assuming a crustal density of 2.3 g/cm^3 for depths up to 1 km and 2.9 g/cm^3 for depths >1 km (Kilburn 2015; Fig. 8). If uncertainties in f_{O_2} and depth constraints are taken into account, liquidus olivine crystallization occurs at a maximum depth near to or just below the Moho (~16 km; Hill and Zucca 1987; Fig. 8). Thus, calculated timescales for KT olivine document magma mixing and storage within the crust (<16 km), perhaps in the volcanic edifice (<10 km; Cayol et al. 2000; Montgomery-Brown et al. 2015; Fig. 8) as has been interpreted for magma storage and transport within the modern Kīlauea plumbing system (e.g., Poland et al. 2014; Pietruszka et al. 2015). Ultimately, diffusion timescales for the KT period are not related to a deeper magmatic history (e.g., ascent from the mantle >17 km), as has been suggested for other Kīlauea eruptions (Rae et al. 2016).

The prehistoric crustal reservoir system

Melt components

Olivine crystals from the KT period preserve both the timing of magma mixing in crustal reservoirs and compositional information about the mixing end members. Four different melt components within the prehistoric reservoir system can be identified from KT olivine based on olivine compositions and their zoning patterns:

1. *Primitive magma*. Normal and shoulder-type zoning occur in high-Fo (e.g., ≥Fo$_{88}$) olivine crystals (black and yellow profiles in Fig. 9a) that grew and were mixed in mantle-derived primitive melt components.
2. *MgO-rich hybrid magma*. Olivine cores and rims with intermediate composition (Fo$_{85–88}$; Fig. 5b, d) grew in

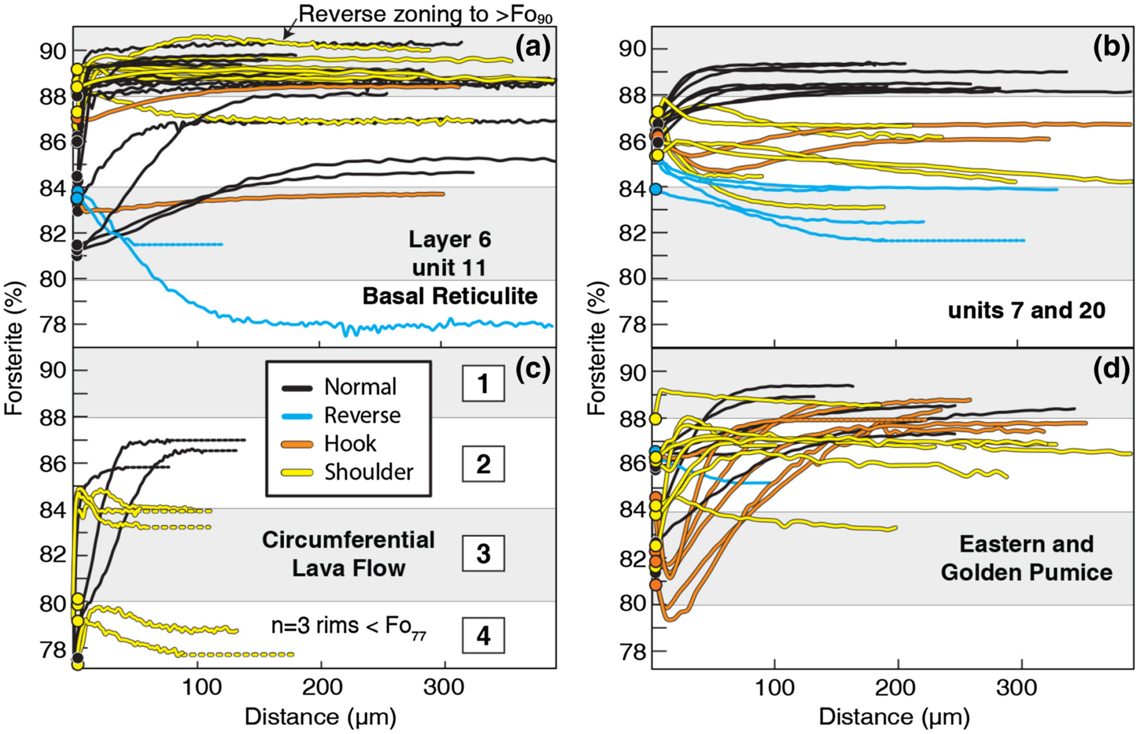

Fig. 9 Olivine forsterite profiles grouped to highlight similar zoning patterns found in multiple samples. Scales are the same in all panels for comparison. *Grey horizontal* regions in each panel help highlight olivine populations as identified in Fig. 3. Zoning styles are distinguished by *color* as in Fig. 6. **a** Most olivine in the first half of the KT (Basal Reticulite, unit 11, Layer 6) are normally zoned with ≥Fo$_{88}$ cores that grew from mantle-derived magmas (melt component [*1*]). The heterogeneity in core and rim Fo suggests sampling of multiple pockets of more evolved magmas (melt components [*2*] and [*3*]). **b** Examples of eruptions with systematic zoning profiles indicative of storage in a reservoir. Almost all profiles are zoned toward a relatively narrow range of rim compositions (Fo$_{85–87.5}$) that probably reflect the hybrid melt (component [*2*]) produced by mixing of primitive and reservoir components (melt components [*1*] and [*3*]). **c** The Circumferential Lava Flow is unique in that its populations all have evolved rims (≤Fo$_{80}$) that record the influence of a low-Mg# magma (melt component [*4*]). *Dashed lines* in the Circumferential Lava Flow panel represent inferred core plateaus based on the similarity between the measured core composition and the end of the geochemical profile. **d** The youngest KT samples (Eastern and Golden Pumice) have mostly complexly zoned olivine profiles. They record mixing of primitive and reservoir components with a low-Mg# melt (component [*4*]), which induced dramatic normal zoning patterns from Fo$_{87–88}$ cores to as low as Fo$_{79–80}$ in the hooks. A final mixing event with a higher-MgO magma produced normal and reverse zoning in shoulder and hook profiles, respectively

or are the result of diffusive re-equilibration within a hybrid melt component that was produced by mixing of primitive and stored magmas.

3. *Evolved reservoir magma*. Reversely zoned crystals with lower Fo cores ($Fo_{80–84}$; Fig. 5b, blue profiles in Fig. 9b) formed within shallower crustal storage levels. This component includes relatively evolved melts produced by fractional crystallization of olivine ± clinopyroxene and plagioclase.
4. *Highly evolved magma*. Strong normal zoning ($Fo_{87–88}$ to $<Fo_{80}$; Fig. 5c, orange profiles in Fig. 9d) in hook profiles was produced by mixing of a primitive melt with a stored, low-Mg# melt component. Evolved olivine cores are also present in minor amounts in early eruption olivine populations (Fig. 3).

Early eruptions (~1500–1670 C.E.)

The types of olivine zoning patterns found within products of individual eruptions can be used to characterize the mixing and storage histories of KT magmas. Olivine populations in early KT eruptions (1500–1650 C.E.; Basal Reticulite, units 7, 11, and 20, and Layer 6) have a wide distribution of core compositions (e.g., $Fo_{78–90}$) dominated by primitive Fo (e.g., $Fo_{87–89}$; Figs. 3, 9a). Normal and shoulder-type zoning profiles with ≥ Fo_{88} core plateaus are most common (e.g., Fig. 9a), suggesting that most of the olivine from these units (up to 90%; Fig. 3) crystallized from mantle-derived magmas (melt component [1]; Fig. 10a). Although this component is clearly recorded by the olivine core compositions, melts sufficiently magnesian to crystallize $Fo_{88–90}$ olivine (>12 wt% MgO) have not been found in KT deposits. The highest glass MgO content measured for the KT period is 11.2 wt% (Helz et al. 2015), which would be in Fe–Mg equilibrium with $Fo_{86–87}$ olivine. This suggests that primitive melts in equilibrium with $Fo_{88–90}$ olivine during the KT period do not reach the surface without some degree of evolution through fractional crystallization and/or magma mixing. Thus, olivine compositions and zoning patterns record a deeper history for KT magmas than that inferred from glass compositions alone.

Some shoulder profiles have reverse zoning to $>Fo_{88}$ (one is reversely zoned up to $Fo_{90.5}$; Fig. 9a). These are interpreted to record mixing of mantle-derived magmas in a lower crustal reservoir, perhaps at 8–10 km near the transition between

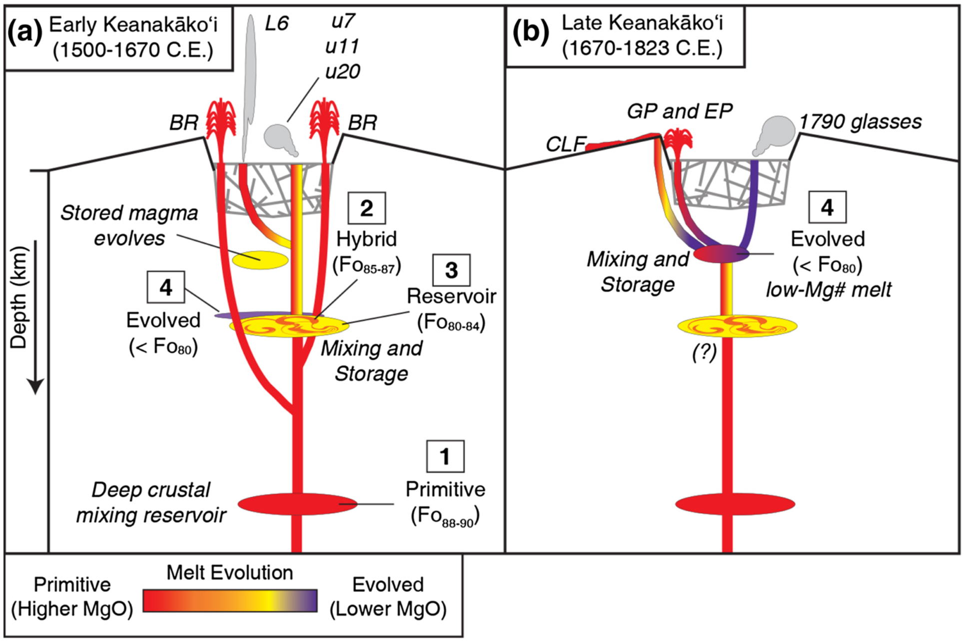

Fig. 10 Simplified cross sections of Kīlauea's summit region depicting the inferred prehistoric plumbing system with crustal mixing and storage regions (not to scale). The stippled region represents caldera collapse breccia infill. Melt component numbers and *colors* are the same as in Fig. 3. The KT is divided into two stages: **a** early eruptions (~1500–1670 C.E.) are dominated by mantle-derived magmas (component [*1*]). Some eruptions are inferred to intersect multiple pockets of magma, producing bimodal and/or heterogeneous olivine populations (components [*2*], [*3*], and [*4*]). Vent locations for the KT period are distributed throughout Kīlauea's summit region (Swanson et al. 2006, 2012b; May et al. 2015), consistent with the interpretation that ascending magmas could have intersected different pockets of melt. **b** Late in the KT (~1670–1820 C.E.), magmas intersected a low-Mg# stored melt (component [*4*]) that strongly influenced the glass (e.g., 1790 eruption; Mucek 2012; Swanson et al. 2014) and olivine compositions. Olivine crystals with hook-type zoning were first stored with the low-Mg# melt component, generating strong normal zoning from $Fo_{87–88}$ to $<Fo_{80}$. A second influx of higher MgO melt generated the thin reversely zoned rims

the volcanic edifice and oceanic crust (Cayol et al. 2000, Montgomery-Brown et al. 2015). A deep origin for >Fo_{88} zoning is also consistent with previous interpretations that melts with >11.0 wt% MgO were probably stored at much deeper levels than the modern summit reservoir system (Helz et al. 2015). Deep crustal storage regions in Kīlauea's modern plumbing system have previously been inferred to explain a lack of earthquake hypocentral locations (Ryan 1988; Denlinger 1997) and a zone of anomalously low velocity material (Lin et al. 2014) near the boundary between the oceanic crust and the volcanic edifice. The compositions and zoning patterns found in KT olivine crystals may provide the first geochemical evidence of deep crustal mixing and storage between ascending mantle-derived magmas before subsequent interaction with evolved magma in shallower reservoirs.

Many eruptions early in the KT period also incorporated more evolved olivine crystals (Figs. 3, 9a, b), which generally have reverse- or hook-style profiles of intermediate and low-Fo composition (e.g., $Fo_{82–88}$). The zoning patterns are diverse with variable profile lengths (10–150 µm) and generally show limited variation in Fo (e.g., 1–4 mol%; Fig. 7). This diversity and the heterogeneous glass MgO contents in many KT units (e.g., 7.0–11.0 wt%; Helz et al. 2015) suggest that ascending magmas may have sampled one or more pockets of stored magmas at shallower depths (melt components [2], [3], and [4]; Fig. 10a). The vent locations for KT eruptions are inferred to be widespread across Kīlauea's summit region (e.g., Swanson et al. 2012b, 2006, May et al. 2015). Thus, ascending magmas could have sampled numerous stored pockets distributed beneath the summit caldera, perhaps as a system of stacked sills (which are structurally favorable after caldera collapse; Corbi et al. 2015).

Normally and reversely zoned olivine crystals from units 7 and 20 (Fig. 9b) define a 'post-mixing' magma storage region where the populations were partially re-equilibrated toward a common melt composition (Fig. 10a). Convergent zoning between olivine populations has been documented in other Kīlauea eruptions (e.g., 1960; Wright and Helz 1996) and has been inferred to reflect mixing of two distinct magmas prior to eruption. Primitive olivine (≥Fo_{88} cores) from melt component [1] mixed with a stored reservoir magma (melt component [3]), generating two olivine populations: one consisting of normally zoned crystals with ≥Fo_{88} plateaus and the other of reversely zoned crystals with $Fo_{82–85}$ plateaus. These reversely zoned olivine and the abundance of olivine cores with $Fo_{83–84}$ (Fig. 3) broadly correspond to the 8.0 wt% MgO peak in glass composition observed by Helz et al. (2015). The two populations were likely stored together because their zoning patterns span similar distances (~200 µm) toward a similar intermediate rim composition (hybrid component, $Fo_{85–87}$; Fig. 9b). Olivine rims with $Fo_{85–87}$ reflect the composition of the hybrid magma created by mixing (e.g., Kahl et al. 2011, 2013; melt component [2]; Fig. 10a), which is consistent with a peak in glass MgO contents at 9.5 wt% and the most magnesian melts measured for the KT period (10–11 wt%; Helz et al. 2015). The complex patterns indicate that pockets of magma within the system reservoir system probably contained many generations of olivine crystals that record more than one mixing event. These eruptions show that at least one shallow storage region in Kīlauea's prehistoric plumbing system may have been repeatedly sampled by ascending KT magmas (Fig. 10a).

Late eruptions (~1670–1820 C.E.)

Olivine from later KT eruptions (Circumferential Lava Flow, Golden and Eastern Pumices; ~1670–1820 C.E.) record additional mixing with a distinct low-Mg# melt (component [4]) that was not sampled before this period (Fig. 10b). The Circumferential Lava Flow (~1670–1700 C.E.; Fig. 9c) preserves populations of olivine from all melt components (Fig. 3) that have either normal or shoulder style profiles zoned toward <Fo_{80} rims (Fig. 9c). Mixing with a higher MgO magma generated the reverse zoning in shoulder profiles (Fig. 9c). A second mixing event with the low-Mg# melt induced normal zoning (1–8 mol% change in Fo) in the outer 5–20 µm of the rim. Olivine cores with <Fo_{80} in the Circumferential Lava Flow (Fig. 9c) may have originated from this component. This low-Mg# component is also recorded in Golden and Eastern Pumices, which have hook-type profiles that decrease to <Fo_{82}, with many recording <Fo_{80} (Fig. 9d). Hook profiles suggest that high-Fo crystals from the primitive component ([1]) were initially mixed with the low-Mg# melt (component [4]), developing 200- to 300-µm-wide normal zoning with 1–10% change in Fo between the core and rim (Fig. 9d). A second mixing event with a more mafic magma (perhaps another intrusion of component [1] or stored reservoir melt components [2] and [3]; Fig. 10b) induced reverse zoning (1–3% Fo) in the thin 5- to 20-µm-wide rims.

The presence of a low-Mg# melt is also confirmed by the glasses from the 1790 C.E. phreatomagmatic eruption (as low as 3.4 wt% MgO; Mucek 2012; Swanson et al. 2014), tephra layers dominated by differentiated glass (e.g., 5.8–6.2 wt% MgO in sample 514 of Mastin et al. 2004; Helz et al. 2014), and rare shards of glass found throughout the tephras with <6.0 wt% MgO (Helz et al. 2014). Incorporation of a low-Mg# component in erupted magmas from ~1670 to 1820 C.E. can explain the large width of zoned regions in olivine (due to contrasts in melt Mg#) and the <Fo_{80} compositions of rims (Circumferential Lava Flow) and hooks (Golden and Eastern Pumices). The low-Mg# melt suggests that some magmas were intruded, but did not erupt early in the KT period (Fig. 10a). Subsequent storage, cooling, and fractional crystallization of the magma resulted in its evolved composition. Alternatively, the low-Mg# component could be a pocket of magma left over from caldera collapse that would have remained isolated and evolved for ~200 years, producing a small volume of evolved melt that was later sampled by ascending KT magmas. This evolved component, in addition to rare shards of orthopyroxene that have low enstatite and Al_2O_3 contents (in sample 419 of Mastin et al. 2004; Helz et al. 2014), probably originated from a strongly evolved melt stored in a shallow region of the plumbing system (Fig. 10b).

Late-stage mixing?

Hook and shoulder olivine zoning patterns (Fig. 5c, d) indicate that some KT magmas were mixed at least twice before eruption. The timing of the later mixing event is difficult to quantify with diffusion models due to the limited spatial resolution (3–6 points using 3–5 µm spacing) and small changes in concentration (~1% for Fo, <0.03 wt% for NiO; Fig. 5c, d) in the compositional reversals. Furthermore, hook and shoulder zoning is typically seen in Fo profiles, but is not as strongly developed in NiO profiles (Fig. 5c). Olivine rims in the hook and shoulder profiles are also generally out of Fe–Mg equilibrium with their surrounding glass (Fig. 7). This disequilibrium is surprising for samples with bimodal olivine populations that are zoned toward the same rim compositions (e.g., unit 7; Figs. 7, 9b), and it suggests that the hybrid melt component may have been unrelated to the magmas that carried the olivine crystals to the surface.

The compositional reversal rims are narrow (5–20 µm), smoothed features without any obvious compositional plateau (Fig. 5c, d; see also Supplementary Material). Thus, they likely reflect late-stage diffusive re-equilibration, albeit limited, from an additional mixing event. This interpretation is consistent with the highly heterogeneous glass MgO contents found within individual tephra layers, which has been interpreted to reflect late-stage mixing of disparate magmas shortly before eruption (Helz et al. 2015). The inefficient mixing of heterogeneous melts may also explain why only some of the KT olivine record thin compositional reversals near the rim. Therefore, the additional mixing event recorded by these rims probably occurred shortly before eruption.

Using numerical diffusion models to simulate the formation of the observed thin rims, we can provide a maximum constraint on how long olivine crystals may have resided within the magmas that carried them to the surface. The calculated Fo content of olivine in Fe–Mg equilibrium with the adhering glass compositions (i.e., the region within the equilibrium field; Fig. 7) can be treated as a boundary condition to determine how long it would take for diffusion to create the outer 5–20 µm observed in the thin rims of hook and shoulder profiles. These numerical models solve the one-dimensional diffusion equation (see Chakraborty 2010 and references therein) and use P, T, and f_{O_2} conditions appropriate for each eruption (Table 3). Model results predict that the 5- to 20-µm-wide olivine rims could have formed by diffusion in a few hours to a few days after mixing (see example in Supplementary Material). Thus, olivine crystals probably resided within the magmas that carried them to the surface for at most a few days before eruption. These timescale constraints demonstrate that the late-stage magmatic histories may have included ascent shortly after mixing, but that most KT magmas had complex mixing and storage histories that preclude simple, rapid ascent to the surface.

Conclusions

Mixing, storage, and diffusive re-equilibration for weeks to years before eruption were key processes controlling Keanakākoʻi Tephra olivine compositions and zoning patterns. These olivine crystals preserve a history of mixing and subsequent storage for weeks to years before eruption. Glass and olivine compositions provide a framework for characterizing the evolution of magma mixing and storage in Kīlauea's prehistoric crustal reservoir system that includes the following:

1. MELTS modeling suggests that at QFM conditions liquidus olivine is only stable at <0.48 GPa, near to the base of the oceanic crust (~16 km). This is consistent with experimental studies, and suggests that mixing and storage probably occurred within the crust. Thus, timescales from KT olivine do not record deeper processes such as ascent from the mantle >40 km as was previously suggested for other Kīlauea eruptions (e.g., Sides et al. 2014; Rae et al. 2016).
2. Diffusion timescales from Fe–Mg and Ni zoning in olivine range from a few weeks to several years and demonstrate that mantle-derived magmas were mixed and stored with relatively evolved reservoir magmas. Thus, the mixing and storage histories for KT magmas are more complex than previously suggested by interpretations of simple rapid ascent and no storage (e.g., Sides et al. 2014).
3. The dominantly normally zoned high-Fo (≥88) olivine populations that occur throughout the ~300 years of the KT represent repeated influx of primitive, mantle-derived magmas (melt component [1]) into Kīlauea's reservoir system. Shoulder-type profiles with reverse zoning to $>Fo_{88}$ provide the first geochemical evidence for mixing and storage of primitive magmas within a deep crustal reservoir at Kīlauea.

4. Melts in equilibrium with >Fo_{88} olivine compositions (11–13 wt% MgO) are conspicuously absent from the current dataset of measured KT glasses (Mucek 2012; Helz et al. 2014, 2015), indicating that KT magmas did not reach the surface without fractional crystallization of olivine and/or magma mixing.
5. Early KT (~1500–1670 C.E.) eruptions were dominated by primitive magmas (component [1]) that sampled a spatially and compositionally heterogeneous crustal reservoir system (melt components [2], [3] and [4]). Bimodal olivine populations with normal and reverse zoning toward intermediate rim compositions ($Fo_{85–87}$) illustrate the establishment of at least one storage region with a hybrid-mixing composition that was repeatedly sampled during the 300+ years of KT volcanism. This hybrid component correlates with a peak in glass MgO contents (9.5 wt%) documented by Helz et al. 2015.
6. A low-Mg# magma (component [4]) incorporated late in the KT (~1670–1820 C.E.) contributed evolved olivine cores and rims to the Circumferential Lava Flow and was responsible for the large Fo range in normally zoned profiles ($Fo_{88–80}$) in the Golden and Eastern pumice units. This interpretation is consistent with low-MgO glasses measured in juvenile material from the 1790 phreatomagmatic eruption (as low as 3.4 wt% MgO).
7. Late-stage mixing recorded by hook and shoulder zoning in olivine crystals throughout the KT may have occurred a few hours to days before eruption. Although their late-stage histories may have included ascent shortly after mixing, most KT magmas had complex mixing and storage histories that preclude simple, rapid ascent to the surface.

Acknowledgements The authors thank Jason Herrin (NTU) and Eric Hellebrand (UH) for support during electron microprobe analyses, Caroline Caplan and Julia Hammer for guidance in electron backscatter diffraction, and Eileen Chen, Scott Milleson, and Valerie Finlayson for assistance with sample preparation. We are grateful to Rosalind Helz and three anonymous reviewers for helping to improve this paper, and thank Gordon Moore for editorial handling. This work was supported by the National Science Foundation (NSF) East Asia and Pacific Summer Institutes grant OISE1513668 in collaboration with the Research Foundation of Singapore, and the Harold T. Stearns Fellowship and the Fred M. Bullard Graduate Fellowship from UH to KL. Additional support was provided by NSF grants EAR1347915 and EAR1449744 to MG, EAR1321890 to TS, and a Singapore Ministry of Education grant (MoE2014-T2-2-041) to FC. This is the University of Hawai‘i School of Ocean and Earth Science and Technology (SOEST) contribution number 10076.

References

Albert H, Costa F, Marti J (2015) Timing of magmatic processes and unrest associated with mafic historical monogenetic eruptions in Tenerife Island. J Petrol 56(10):1945–1966. doi:10.1093/petrology/egv058

Armstrong JT (1988) Quantitative analyses of silicate and oxide materials: comparison of Monte Carlo, ZAF, and φ(ρz) procedures. Microbeam analyses. San Francisco Press, San Francisco, pp 239–246

Cardozo N, Allmendinger RW (2013) Spherical projections with OSXStereonet. Comput Geosci 51:193–205. doi:10.1016/j.cageo/2012.07.021

Cayol V, Dieterich JH, Okamura AT, Miklius A (2000) High magma storage rates before the 1983 eruption of Kilauea, Hawaii. Science 288(5475):2343–2346. doi:10.1126/science.288.5475.2343

Cervelli PF, Miklius A (2003) The shallow magmatic system of Kīlauea volcano. In: Heliker C, Swanson DA, Takahashi TJ (eds) The Pu‘u ‘Ō‘ō-Kūpianaha eruption of Kīlauea Volcano, Hawai‘i; the first 20 years. US Geological Survey, Washington, DC, pp 149–163

Chakraborty S (2010) Diffusion coefficients in olivine, wadsleyite and ringwoodite. Rev Miner Geochem 72:603–639

Clague DA, Denlinger RP (1994) Role of olivine cumulates in destabilizing the flanks of Hawaiian volcanoes. Bull Volc 56:425–434

Clague D, Moore JG, Dixon JE, Friesen WB (1995) Petrology of submarine lavas from Kilauea's Puna Ridge, Hawaii. J Petrol 36(2):299–349. doi:10.1093/petrology/36.2.299

Corbi F, Rivalta E, Pinel V, Maccaferri F, Bagnardi M, Acocella V (2015) How caldera collapse shapes the shallow emplacement and transfer of magma in active volcanoes. Earth Planet Sci Lett 431:287–293. doi:10.1016/j.epsl.2015.09.028

Costa F, Chakraborty S (2004) Decadal time gaps between mafic intrusion and silicic eruption obtained from chemical zoning patterns in olivine. Earth Planet Sci Lett 224:517–530. doi:10.1016/j.epsl/2004.08.011

Costa F, Dungan M (2005) Short time scales of magmatic assimilation from diffusion modeling of multiple elements in olivine. Geology 33(10):837–840. doi:10.1130/G21675.1

Costa F, Dohmen R, Chakraborty S (2008) Time scales of magmatic processes from modeling the zoning patterns of crystals. Rev Miner Geochem 69(1):545–594. doi:10.2138/rmg.2008.69.14

Davis FA, Cottrell E, Birner SK, Warren J, Lopez OG (2017) Revisiting the electron microprobe method of spinel-olivine-orthopyroxene oxybarometry applied to spinel peridotites. Am Mineral 102:421–435. doi:10.2138/am-2017-5823

Denlinger RP (1997) A dynamic balance between magma supply and eruption rate at Kilauea volcano, Hawaii. J Geophys Res 102(B8):18091–18100. doi:10.1029/97JB01071

Dohmen R, Chakraborty S (2007a) Fe-Mg diffusion in olivine II: point defect chemistry, change of diffusion mechanisms and a model for calculation of diffusion coefficients in natural olivine. Phys Chem Miner 34(6):409–430. doi:10.1007/s00269-007-0158-6

Dohmen R, Chakraborty S (2007b) Erratum on "Fe–Mg diffusion in olivine II: point defect chemistry, change of diffusion mechanisms and a model for calculation of diffusion coefficients in natural olivine". Phys Chem Miner 34:597–598. doi:10.1007/s00269-007-0185-3

Donovan JJ, Tingle TN (1996) An improved mean atomic number correction for quantitative microanalysis. J Microsc 2(1):1–7. doi:10.1017/S1431927696210013

Easton RM (1987) Stratigraphy of Kilauea Volcano. In: Decker RW, Wright TL, Stauffer PH (eds) Volcanism in Hawaii. US Geological Survey, Washington, DC, pp 243–260

Easton RM, Garcia MO (1980) Petrology of the Hilina Formation, Kilauea Volcano, Hawaii. Bull Volcanol 43(4):657–673. doi:10.1007/BF02600364

Eggins SM (1991) Petrogenesis of Hawaiian tholeiites: 1, phase equilibria constraints. Contrib Miner Petrol 110:387–397. doi:10.1007/BF00310752

Ellis W (1827) Narrative of a tour through Hawaii, or, Owyhee; with observations on the natural history of the Sandwich Islands, and remarks on the manners, customs, traditions, history, and language of their inhabitants, 2nd edn. H. Fisher, Son, and P. Jackson, London, p 515

Garcia MO (2015) How and why Hawaiian volcanism has become pivotal to our understanding of volcanoes from their source to the surface. In: Carey R, Cayol V, Poland M, Weis D (eds) Hawaiian volcanoes: from source to surface. American Geophysical Union, Washington, DC, pp 1–18. doi:10.1002/9781118872079.ch1

Gavrilenko M, Ozerov A, Kyle PR, Carr MJ, Nikulin A, Vidito C, Danyushevsky L (2016) Abrupt transition from fractional crystallization to magma mixing at Gorely volcano (Kamchatka) after caldera collapse. Bull Volcanol 78:1–47. doi:10.1007/s00445-016-1038-z

Ghiorso MS, Gualda GAR (2015) An H_2O-CO_2 mixed fluid saturation model compatible with rhyolite-MELTS. Cont Min Petrol 169(53):1–30. doi:10.1007/s00410-015-1141-8

Girona T, Costa F (2013) DIPRA: a user-friendly program to model multi-element diffusion in olivine with applications to timescales of magmatic processes. Geochem Geophys Geosys 14(2):422–431. doi:10.1029/2012GC004427

Gualda GAR, Ghiorso MS, Lemons RV, Carley T (2012) Rhyolite-MELTS: a modified calibration of MELTS optimized for silica-rich, fluid bearing magmatic systems. J Petrol 53(5):875–890. doi:10.1093/petrology/egr080

Hartley ME, Morgan DJ, Maclennan J, Edmonds M, Thordarson T (2016) Tracking timescales of short-term precursors to large basaltic fissure eruptions through Fe-Mg diffusion in olivine. Earth Planet Sci Lett 439:58–70. doi:10.1016/j.epsl/2016.01.018

Helz RT (1987) Diverse olivine types in lava of the 1959 eruption of Kilauea Volcano and their bearing on eruption dynamics. In: Decker RW, Wright TL, Stauffer PH (eds) Volcanism in Hawaii. US Geological Survey, Washington, DC, pp 691–722

Helz RT, Thornber CR (1987) Geothermometry of Kilauea Iki lava lake, Hawaii. Bull Volcanol 49(5):651–668. doi:10.1007/BF01080357

Helz RT, Clague DA, Mastin LG, Rose TR (2014) Electron microprobe analyses of glasses from Kīlauea tephra units, Kīlauea Volcano, Hawaii. US Geol Surv Open File Rep 2014–1090:24. doi:10.3133/ofr20141090

Helz RT, Clague DA, Mastin LG, Rose TR (2015) Evidence for large compositions ranges in coeval melts erupted from Kīlauea's summit reservoir. In: Carey R, Cayol V, Poland M, Weis D (eds) Hawaiian volcanoes: from source to surface. American Geophysical Union, Washington, DC, pp 125–145. doi:10.1002/9781118872079.ch7

Helz RT, Cottrell E, Brounce MN, Kelley KA (2017) Olivine-melt relationships and syneruptive redox variations in the 1959 eruption of Kīlauea Volcano as revealed by XANES. J Volc Geotherm Res 333-334:1-14. doi:10.1016/j.jvolgeores.2012.12.006

Hill DP, Zucca JJ (1987) Geophysical constraints on the structure of Kilauea and Mauna Loa volcanoes and some implications for seismomagmatic processes. In: Decker RW, Wright TL, Stauffer PH (eds) Volcanism in Hawaii. US Geological Survey, Washington, DC, pp 903–917

Jarosewich E, Nelen JA, Norberg JA (1980) Reference samples for electron microprobe analysis. Geos News 4(1):43–47. doi:10.1111/j.1751-908X.1980.tb00273.x

Kahl M, Chakraborty S, Costa F, Pompilio M (2011) Dynamic plumbing system beneath volcanoes revealed by kinetic modeling, and the connection to monitoring data: an example from Mt. Etna. Earth Planet Sci Lett 308(1–2):11–22. doi:10.1016/j.epsl.2011.05.008

Kahl M, Charaborty S, Costa F, Pompilio M, Luizzo M, Viccaro M (2013) Compositionally zoned crystals and real-time degassing data reveal changes in magma transfer dynamics during the 2006 summit eruptive episodes of Mt. Etna. Bull Volcanol 75:1–14

Kilburn CRJ (2015) Lava flow hazards and modeling. In: Sigurdsson H, Houghton B, McNutt SR, Rymer H, Stix J (eds) The encyclopedia of volcanoes. The Academic Press, San Diego, pp 957–934

Lin G, Amelung F, Lavallée Y, Okubo PG (2014) Seismic evidence for a crustal magma reservoir beneath the upper east rift zone of Kilauea volcano, Hawaii. Geology 42(3):187–190. doi:10.1130/G35001.1

Mastin LG (1997) Evidence for water influx from a caldera lake during the explosive hydromagmatic eruption of 1790, Kilauea Volcano, Hawaii. J Geophys Res 102(B9):20093–20109. doi:10.1029/97JB01426

Mastin LG, Christiansen RL, Thornber C, Lowenstern J, Beeson M (2004) What makes hydromagmatic eruptions violent? Some insights from the Keanakāko'i Ash, Kīlauea Volcano, Hawai'i. J Volcanol Geotherm Res 137(1–3):15–31. doi:10.1016/j.jvolgeores.2004.05.015

Matzen AK, Baker MB, Beckett JR, Stolper EM (2011) Fe–Mg partitioning between olivine and high-magnesian melts and the nature of Hawaiian parental liquids. J Petrol 52:1243–1263. doi:10.1093/petrology/egq089

May M, Carey RJ, Swanson DA, Houghton BF (2015) Reticulite-producing fountains from ring fractures in Kīlauea Caldera ca. 1500 CE. In: Carey R, Cayol V, Poland M, Weis D (eds) Hawaiian volcanoes: from source to surface. American Geophysical Union, Washington, DC, pp 351–367. doi:10.1002/9781118872079.ch16

McPhie J, Walker JP, Christiansen RL (1990) Phreatomagmatic and phreatic fall and surge deposits from explosions at Kilauea volcano, Hawaii, 1790 A.D.: Keanakakoi Ash Member. Bull Volcanol 52(5):334–354. doi:10.1007/BF00302047

Montgomery-Brown EK, Poland MP, Miklius A (2015) Delicate balance of magmatic-tectonic interaction at Kīlauea Volcano, Hawai'i, revealed from slow slip events. In: Carey R, Cayol V, Poland M, Weis D (eds) Hawaiian volcanoes: from source to surface. American Geophysical Union, Washington, DC, pp 269–288. doi:10.1002/9781118872079.ch13

Moussallam Y, Edmonds M, Scaillet B, Peters N, Gennaro E, Sides I, Oppenheimer C (2016) The impact of degassing on the oxidation state of basaltic magmas: a case study of Kīlauea volcano. Earth Planet Sci Lett 450:317–325. doi:10.1016/j.epsl.2016.06.031

Mucek A (2012) Geochemistry of glasses from the Keanakāko'i Tephra. Bachelor of Science Senior Thesis, submitted to the University of Hawai'i at Mānoa

Neal CA, Lockwood JP (2003) Geologic map of the summit region of Kilauea Volcano, Hawaii. U.S. Geol Surv Investigations Series I-2759. https://pubs.usgs.gov/imap/i2759/. Accessed 01 Jan 2017

Petry C, Chakraborty S, Palme H (2004) Experimental determination of Ni diffusion coefficients in olivine and their dependence on temperature, composition, oxygen fugacity, and crystallographic orientation. Geochim Cosmochim Acta 68(20):4179–4188. doi:10.1016/j.gca.2004.02.024

Pietruszka AJ, Heaton DE, Marske JP, Garcia MO (2015) Two magma bodies beneath the summit of Kīlauea Volcano unveiled by isotopically distinct melt deliveries from the mantle. Earth Planet Sci Lett 413:90–100. doi:10.1016/j.epsl.2014.12.040

Poland MP, Miklius A, Montgomery-Brown E (2014) Magma supply, storage, and transport at shield-stage Hawaiian volcanoes. In: Poland MP, Takahashi TJ, Landowski CM (eds) Characteristics of Hawaiian volcanoes. US Geological Survey, Washington, DC, pp 179–234. doi:10.3133/pp18015

Prior DJ, Boyle AP, Brenker F, Cheadle MC, Day A, Lopez G, Peruzzo L, Potts GJ, Reddy S, Spiess R, Timms NE, Trimby P, Wheeler J, Zetterström L (1999) The application of electron backscatter diffraction and orientation contrast imaging in the SEM to textural problems in rocks. Am Mineral 84:1741–1759. doi:10.2138/am-1999-11-1204

Rae ASP, Edmonds M, Maclennan J, Morgan D, Houghton B, Hartley ME, Sides I (2016) Time scales of magma transport and mixing at Kīlauea Volcano, Hawai'i. Geology 44(6):463–466. doi:10.1130/G37800.1

Rhodes JM, Vollinger MJ (2005) Ferric-ferrous ratios in the 1984 Mauna Loa lavas: a contribution to understanding the oxidation state of Hawaiian magmas. Contrib Miner Petrol 149:666–674. doi:10.1007/s00410-005-0662-y

Roeder PL, Emslie RF (1970) Olivine-liquid equilibrium. Contr Miner Petrol 29:275–289. doi:10.1007/BF00371276

Ryan MP (1988) The mechanics and three-dimensional internal structure of active magmatic systems: Kilauea Volcano, Hawaii. J Geophys Res 93(5):4213–4248. doi:10.1029/JB093iB05p04213

Sharp RP, Dzurisin D, Malin MC (1987) An early 19th century reticulite pumice from Kilauea Volcano. In: Decker RW, Wright TL, Stauffer PH (eds) Volcanism in Hawaii. US Geological Survey, Washington, DC, pp 395–404

Shea T, Costa F, Krimer D, Hammer JE (2015a) Accuracy of timescales retrieved from diffusion modeling in olivine: a 3D perspective. Am Mineral 100:2026–2042. doi:10.2138/am-2015-5163

Shea T, Lynn KJ, Garcia MO (2015b) Cracking the olivine zoning code: distinguishing between crystal growth and diffusion. Geology 43(10):935–938. doi:10.1130/G37082.1

Sides IR, Edmonds M, Maclennan J, Swanson DA, Hougton BF (2014) Eruption style at Kīlauea Volcano in Hawai'i linked to primary melt composition. Nat Geosci 7:464–469. doi:10.1038/ngeo2140

Swanson DA (2008) Hawaiian oral tradition describes 400 years of volcanic activity at Kīlauea. J Volcanol Geotherm Res 176(3):427–431. doi:10.1016/j.jvolgeores.2008.01.033

Swanson DA, Rose TR, Fiske RS (2006) The layer 6 scoria fall about 400 years ago at Kilauea. EOS Am Geophys Union Trans 87:V33B–0646

Swanson DA, Rose TR, Fiske RS, McGeehin JP (2012a) Keanakāko'i Tephra produced by 300 years of explosive eruptions following collapse of Kīlauea's caldera in about 1500 CE. J Volcanol Geotherm Res 215–216:8–25. doi:10.1016/j.jvolgeorres.2011.11.009

Swanson DA, Zolkos SP, Haravitch B (2012b) Ballistic blocks around Kīlauea Caldera: their vent locations and number of eruptions in the late 18th century. J Volcanol Geotherm Res 231–232:1–11. doi:10.1016/j.jvolgeores.2012.04.008

Swanson DA, Rose TR, Mucek AE, Garcia MO, Fiske RS, Mastin LG (2014) Cycles of explosive and effusive eruptions at Kīlauea Volcano, Hawai'i. Geology 42(7):631–634. doi:10.1130/G35701.1

Swanson DA, Weaver SJ, Houghton BF (2015) Reconstructing the deadly eruptive events of 1790 CE at Kīlauea Volcano, Hawai'i. GSA Bull 127(3–4):503–515. doi:10.1130/B31116.1

Swanson DA, Biass S, Garcia M (2017) End of an era: the final explosive eruptions of Keanakāko'i Tephra at Kīlauea. In: GSA Cordilleran Meeting, pp 43–46

Tilling RI, Dvorak JJ (1993) Anatomy of a basaltic volcano. Nature 363(6425):125–133

Wagner TP, Grove TL (1998) Melt/harzburgite reaction in the petrogenesis of tholeiitic magma from Kilauea volcano, Hawaii. Contrib Miner Petrol 131:1–12. doi:10.1007/s004100050374

Wright TL, Helz RT (1996) Differentiation and magma mixing on Kilauea's east rift zone: a further look at the eruptions of 1955 and 1960. Part II. The 1960 lavas. Bull Volcanol 57:602–630. doi:10.1007/s004450050115